CrossMark

Large extracellular space leads to neuronal susceptibility to ischemic injury in a Na^+/K^+ pumps–dependent manner

Niklas Hübel[1] · R. David Andrew[2] · Ghanim Ullah[1]

© Springer Science+Business Media New York 2016

Abstract The extent of anoxic depolarization (AD), the initial electrophysiological event during ischemia, determines the degree of brain region–specific neuronal damage. Neurons in higher brain regions exhibiting nonreversible, strong AD are more susceptible to ischemic injury as compared to cells in lower brain regions that exhibit reversible, weak AD. While the contrasting ADs in different brain regions in response to oxygen–glucose deprivation (OGD) is well established, the mechanism leading to such differences is not clear. Here we use computational modeling to elucidate the mechanism behind the brain region–specific recovery from AD. Our extended Hodgkin–Huxley (HH) framework consisting of neural spiking dynamics, processes of ion accumulation, and ion homeostatic mechanisms unveils that glial–vascular K^+ clearance and Na^+/K^+–exchange pumps are key to the cell's recovery from AD. Our phase space analysis reveals that the large extracellular space in the upper brain regions leads to impaired Na^+/K^+–exchange pumps so that they function at lower than normal capacity and are unable to bring the cell out of AD after oxygen and glucose is restored.

Action Editor: J. Rinzel

✉ Niklas Hübel
niklas.huebel@gmail.com

[1] Department of Physics, University of South Florida, Tampa, FL 33620, USA

[2] Department of Biomedical and Molecular Sciences, Queen's University, Kingston, ON, Canada

1 Introduction

Anoxic depolarization (AD) is characterized as a sudden and profound loss of membrane potential that drains residual stored energy in compromised gray matter. *In vivo*, temporary global ischemia can lead to the electrophysiological event of AD (Dijkhuizen et al. 1999; Murphy et al. 2008). The susceptibility of neurons to injury from AD depends crucially on the brain region (Falini et al. 1998; Luigetti et al. 2012). Brainstem neurons have a good chance to fully recover after normal blood flow is restored. In higher brain regions, however, cells remain depolarized and can get severely damaged in a stroke–like scenario (Falini et al. 1998; Luigetti et al. 2012).

This distinctly different behavior is also found in brain slice experiments, in which oxygen–glucose deprivation (OGD) is used to trigger AD (Brisson and Andrew 2012; Brisson et al. 2013; Brisson et al. 2014). Such isolated cortex preparations rule out local differences in blood flow as a cause for the observed phenomenon. Brain slice experiments confirm that hypothalamic neurons are intrinsically more resistant to injury and are more likely to exhibit recoverable AD (Fig. 1a). In contrast, the thalamus and neocortex show high vulnerability and permanent depolarization that fails to recover after oxygen–glucose is restored (Fig. 1b). The thalamic–hypothalamic interface marks the boundary between tissue that is susceptible to ischemic injury and tissue that is resistant (Brisson et al. 2013). The mechanism leading to neuronal failure to recover from AD in the upper
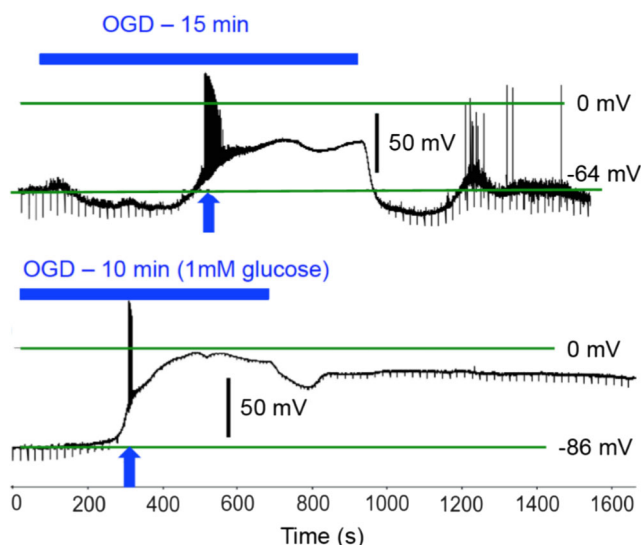
Fig. 1 Observed membrane potential during and after OGD. In the hypothalamus (*upper trace*), the neuron recovers and repolarizes right after normal oxygen and glucose supply is restored. In the thalamus (*lower trace*), the cells remain depolarized. The plots are adopted from Brisson and Andrew (2012) with permission

brain regions remains incompletely understood.

AD is only one example of a pathology that goes along with huge changes of ion concentrations in the neural microenvironment (Centonze et al. 2001; Somjen 2004). Others are seizure–like bursting activity and spreading depolarizations (SD) (Kager et al. 2000, 2007; Cressman Jr. et al. 2009, 2011; Krishnan and Bazhenov 2011; Ingram et al. 2014; Wei et al. 2014a, Hansen and Zeuthen 1981; Hübel and Dahlem 2014; Somjen 2004). All of these dynamics can be studied in surprisingly simple mathematical models. Already, single cell Hodgkin–Huxley–based neuron models with dynamical ion concentrations in two spatial compartments—the intracellular (ICS) and extracellular (ECS) spaces—exhibit all of these pathologies (Hübel and Dahlem 2014; Wei et al. 2014a; Ullah and Schiff 2009, 2010; Ullah et al. 2015). So even such reduced models seem to capture the essential mechanisms that govern neural ion dynamics.

The mathematical structure of single neuron models is well understood and it is possible to determine exact parameter ranges for epileptic seizure dynamics, SD, and permanent depolarization which leads to cell injury (Hübel and Dahlem 2014; Ullah et al. 2015). The earlier computational studies involving ion dynamics of single neurons focused independently on epilepsy (Cressman Jr. et al. 2009, 2011; Barreto and Cressman 2010; Bazhenov et al. 2004; Frohlich and Bazhenov 2006), SD (Kager et al. 2000), and AD (Zandt et al. 2011; Dahlem et al. 2014; Hübel et al. 2014). The richness of dynamical behaviors that is seen in

one neuron model—showing different types of oscillations and fixed points—has been pointed out early (Cressman Jr. et al. 2009, 2011; Barreto and Cressman 2010) and has been explored in more detail recently (Hübel and Dahlem 2014; Ullah et al. 2015; Wei et al. 2014a). Neural processes ranging from normal spiking to pathologies like seizures, SD, and AD can be described simultaneously in a single model.

While some studies have dealt with AD scenarios in single cell models before, a systematic study of recovery requirements after ischemia– or OGD–induced depolarization has not been performed yet, which is the subject of this paper. We here investigate the effect of the volume fraction between the ECS and the ICS on the model dynamics. It has been shown already that under certain conditions a large ECS may inhibit recovery from AD and lead to permanent depolarization (Ullah et al. 2015), and also that the size of the ECS may affect the susceptibility to SD–like depolarizations (Barreto and Cressman 2010). From the macroscopic perspective, changing the size of the ECS or the extracellular volume fraction, which is defined as the fraction of ECS in whole tissue consisting of neurons, glia cells, and the space between, corresponds to different cell packing or cell density. This is a brain region–dependent tissue property (Schüz and Palm 1989; Herculano-Houzel and Lent 2005; Collins et al. 2010).

In the model, temporary OGD depolarizes the membrane and causes the breakdown of ion gradients. Cells with a normal ECS recover after restoring normal oxygen–glucose supply while cells with a large ECS do not. We use a recently developed method of threshold analysis (Hübel and Dahlem 2014) to determine the point of recovery failure—and its nature.

The model predicts that for a larger extracellular volume fraction, the depolarized state tolerates lower concentrations of extracellular K^+. This implies a higher K^+ clearance demand by the vasculature or glia cells and weaker activity of the Na^+/K^+–exchange pumps at the threshold. For SD it has been shown both theoretically and experimentally that vascular K^+ regulation has a much stronger recovery effect on depolarized neurons than the ion pumps (Hübel et al. 2014; Hübel and Dahlem 2014; Hoffmann et al. 2012; Sukhotinsky et al. 2010). Theoretically, even fully restored pump activity is not sufficient for recovering neurons from their depolarized condition (Hübel et al. 2014; Hübel and Dahlem 2014). Instead, temporary uptake of potassium by glia cells or the vasculature are vital mechanisms without which the cells would remain dysfunctional. Experimentally, this is reflected in the observation that blood pressure is inversely related to the duration of SD, while enhanced tissue oxygenation—implying stronger pump activity—has almost no effect (Hoffmann et al. 2012; Sukhotinsky et al. 2010). These theoretical and experimental studies show that

vascular coupling can enhance recovery effectively, while modifying the rate of pump activity within a certain range does not change the course of events. The recovery failure scenario in our model gives us a more precise picture of the relative recovery contribution of pumps and other regulation. It shows how recovery from AD is a combined effort of the pumps and vascular coupling. Impairment of either can lead to permanent depolarization. By investigating the reason for recovery failure, we also gain new insights on general properties of the recovery point at which the neuron repolarizes. This enables us to prove in a final remark that recovery fundamentally comes down to a bifurcation of the membrane state.

2 Mathematical neuron model

We consider a simple Hodgkin–Huxley–based model for neural ion dynamics. The full system comprises of the ICS and the ECS that are separated by the neural membrane. Different concentrations of Na$^+$, K$^+$ and Cl$^-$ ions in these compartments characterize the neural microenvironment under normal physiological conditions.

Transmembrane currents induce changes in ion concentrations. Ion pumps maintain the ion gradients. In addition to that, glia cells and the vascular system regulate the extracellular K$^+$ concentration. We refer to the latter as ion exchange with external (glial or vascular) reservoirs. The same model was used by Hübel and Dahlem (2014) and the setup is schematically summarized in Fig. 2.
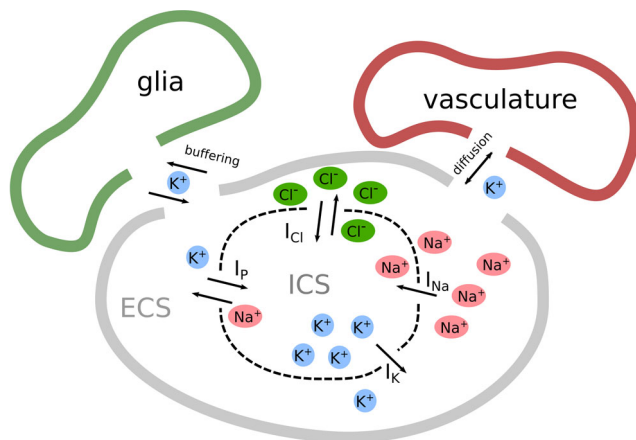

Fig. 2 The neuron model consists of two spatial compartments, the ICS and ECS. The neural membrane (dashed black line) separates the compartments. Na$^+$, K$^+$, and Cl$^-$ ions are present inside and outside of the cell in different concentrations. Transmembrane ion currents (I_{Na}, I_K, and I_{Cl}) and the K$^+$/Na$^+$–exchange pumps (current I_p) transport ions across the membrane. In addition, K$^+$ can be buffered by glia cells or diffuse into the vascular system, which are both external reservoirs

2.1 The membrane model

The electrical properties of the membrane are described in terms of an equivalent electrical circuit. In this picture a capacitance C_m is assigned to the neural membrane. The dynamics of the membrane potential V is governed by the three currents I_{ion} (for $ion \in \{K, Na, Cl\}$) through ion channels, and a pump current I_p accounting for the Na$^+$/K$^+$–exchange that is needed to maintain the physiological equilibrium (see below).

According to the Hodgkin–Huxley (HH) formalism, the channel conductances for K$^+$ and Na$^+$ depend on the gating variables n (K$^+$ activation), m (Na$^+$ activation), and h (Na$^+$ inactivation) (Hodgkin 1948: Hodgkin and Huxley 1952a, b, c; Hodgkin et al 1952) These variables describe the voltage–dependent opening probabilities of the channels. The m–gate responds extremely fast to variations of the membrane potential and can thus be approximated adiabatically by setting $m = m_\infty$ (see below). The full list of membrane rate equations reads

$$\frac{dV}{dt} = -\frac{1}{C_m}(I_{Na} + I_K + I_{Cl} + I_p), \tag{1}$$

$$\frac{dn}{dt} = \phi\frac{n_\infty - n}{\tau_n}, \tag{2}$$

$$\frac{dh}{dt} = \phi\frac{h_\infty - h}{\tau_h}. \tag{3}$$

They contain the membrane capacitance C_m and a timescale parameter ϕ. The asymptotic values x_∞ and timescale functions τ_x for $x \in \{n, m, h\}$ are given by

$$x_\infty = \frac{\alpha_x}{\alpha_x + \beta_x}, \tag{4}$$

$$\tau_\infty = \frac{1}{\alpha_x + \beta_x}, \tag{5}$$

with the HH exponential functions

$$\alpha_n = \frac{0.01(V + 34)}{1 - \exp(-(V + 34)/10)}, \tag{6}$$

$$\beta_n = 0.125\exp(-(V + 44)/80), \tag{7}$$

$$\alpha_m = \frac{0.1(V + 30)}{1 - \exp(-(V + 30)/10)}, \tag{8}$$

$$\beta_m = 4\exp(-(V + 55)/18), \tag{9}$$

$$\alpha_h = 0.07\exp(-(V + 44)/20), \tag{10}$$

$$\beta_h = \frac{1}{1 + \exp(-(V + 14)/10)}. \tag{11}$$

The channel conductances g_{ion} depend on the gating variables in the following way

$$g_K = g_K^l + g_K^g n^4, \tag{12}$$

$$g_{Na} = g_{Na}^l + g_{Na}^g m^3 h, \tag{13}$$

$$g_{Cl} = g_{Cl}^l, \tag{14}$$

Table 1 Model parameters

Name	Value & unit	Description
C_m	1 μF/cm^2	membrane capacitance
ϕ	3/msec	time scale parameter
g_{Na}^l	0.0175 mS/cm^2	Na$^+$ leak cond.
g_{Na}^g	100 mS/cm^2	max. gated Na$^+$ cond.
g_K^l	0.05 mS/cm^2	K$^+$ leak cond.
g_K^g	40 mS/cm^2	max. gated K$^+$ cond.
g_{Cl}^l	0.02 mS/cm^2	Cl$^-$ leak cond.
ω_i	2,160 μm^3	ICS volume
ω_e	720 μm^3	normal ECS volume
F	96,485 C/mol	Faraday's constant
A_m	922 μm^2	membrane surface area
γ	9.6e–2 μm$^3 \frac{\text{mM}}{\text{msec}} \frac{\text{cm}^2}{\mu\text{A}}$	conversion factor
ρ	6.8 μA/cm^2	max. pump current
λ	3e–2/sec	diffusion strength
K_{bath}	4 mM	K$^+$ conc. bath

where g_{ion}^l is a small leak conductance and g_{ion}^g is the much larger maximal conductance of the voltage–gated channels. We only consider a leak current for Cl$^-$. With these conductances the channel currents are

$$I_{ion} = g_{ion}(V - E_{ion}) . \tag{15}$$

They depend on the concentration– and charge–dependent Nernst potentials

$$E_{ion} = \frac{26.64}{z_{ion}} \ln(ion_e/ion_i) \tag{16}$$

with the ion valence z_{ion} and concentrations $ion_{i/e}$ for $ion \in \{Na, K, Cl\}$. Model parameters are found in Table 1.

Using a HH membrane description is the paradigmatic and simplest possible ansatz to describe neural ion dynamics. We would like to remark that particularly in the context of epilepsy and SD much more detailed membrane models exist (Kager et al. 2000, 2002; Bazhenov et al. 2004; Yao et al. 2011; Shandilya and Timme 2011). However, it has been shown that the general mathematical structure of ion–based neuron models that we review below is largely independent of the specific choice of ion channels and gating dynamics (Hübel et al. 2014; Hübel and Dahlem 2014).

2.2 Ion dynamics

In the original HH model ion concentrations and Nernst potentials are model parameters that do not change. If we want to study actual ion dynamics we must take into account that the transmembrane ion currents induce changes in ion concentrations. To compute these changes, currents must be be converted to ion fluxes by a factor

$$\gamma = \frac{A_m}{F} , \tag{17}$$

which contains the membrane surface area A_m and Faraday's constant F. The ion fluxes must then be divided by the volume ω_i or ω_e (ICS or ECS respectively) of the relevant compartment.

Recall that we have included a pump current to the first HH Eq. (1). Pumps are necessary, because physiological resting conditions are characterized by large ion gradients, i.e., concentration differences between ICS and ECS, for Na$^+$ and K$^+$. To maintain these gradients, ion pumps exchange intracellular Na$^+$ for extracellular K$^+$, which is done at a 3/2–ratio. The rate equations for ion concentrations in the ICS are

$$\frac{dK_i}{dt} = -\frac{\gamma}{\omega_i}(I_{K^+} - 2I_p) , \tag{18}$$

$$\frac{dNa_i}{dt} = -\frac{\gamma}{\omega_i}(I_{Na^+} + 3I_p) , \tag{19}$$

$$\frac{dCl_i}{dt} = +\frac{\gamma}{\omega_i}I_{Cl^-} . \tag{20}$$

The pump current I_p increases with Na_i and K_e (Cressman Jr. et al. 2009):

$$I_p = \rho \left(1 + \exp\left(\frac{25 - Na_i}{3} \right) \right)^{-1}$$
$$\left(1 + \exp(5.5 - K_e) \right)^{-1} \tag{21}$$

I_p saturates to a maximum level only when both, Na_i and K_e, are high. Under physiological resting conditions the pump operates at about 10% of the maximal pump rate ρ (Attwell and Laughlin 2001).

Electroneutrality is an important symmetry of the model, and it implies that the intracellular charge concentration

$$Q_i := Na_i + K_i - Cl_i = Na_i^0 + K_i^0 - Cl_i^0 \tag{22}$$

is constant. Accordingly Na_i, K_i and Cl_i are not independent, and one of the rate Eqs. (18)–(20) can be replaced by simply solving Eq. (22) for that variable. Note that initial physiological resting conditions are denoted by a superscript 0.

Also mass conservation holds and ion concentrations in the ECS follow from values in the ICS by solving the following constraint equations:

$$Na_i\omega_i + \text{Na}_e\omega_e = Na_i^0\omega_i + \text{Na}_e^0\omega_e , \tag{23}$$

$$K_i\omega_i + \text{K}_e\omega_e = K_i^0\omega_i + \text{K}_e^0\omega_e + \Delta\text{N}^K , \tag{24}$$

$$Cl_i\omega_i + \text{Na}_e\omega_e = Cl_i^0\omega_i + Cl_e^0\omega_e . \tag{25}$$

We have added the quantity ΔN^K in Eq. (24). It accounts for changes of the K^+ content of the system due to particle exchange with external reservoirs. These reservoirs can be the vasculature or glia cells, which both play an important role in regulating the extracellular K^+ level. A positive/negative value of ΔN^K corresponds to K^+ gain/loss in the system.

Of course, Na^+ and Cl^- can also be exchanged with external reservoirs, but the pathologies we study here are most prominently characterized by a huge rise of K^+ in the ECS. Most studies emphasize the role of K^+ regulation, but a generalization to the other ions would be straightforward.

The type of reservoir coupling—vascular or glial—determines the dynamics of ΔN^K. For simplicity we only consider diffusive coupling to the vasculature in this study. It has been shown that including glial buffering does not lead to qualitatively different results (Hübel and Dahlem 2014) and also in the here presented study the specific process of K^+ reduction is irrelevant to explain the observed behavior (see below).

To model vascular coupling, we assume that the blood vessels provide an external bath to and from which K^+ can diffuse. The defining parameters in this scheme are the K^+ concentration of the bath K_{bath} and the coupling strength λ. The dynamics of ΔN^K is then proportional to the diffusive flux J_{diff}:

$$J_{diff} = \lambda (K_{bath} - K_e) , \tag{26}$$

$$\frac{d\Delta N^K}{dt} = \omega_e J_{diff} . \tag{27}$$

Note that in this model the K^+ uptake capacity of the vascular bath is unlimited.

In summary, the whole system is defined by the three membrane rate Eqs. (1)–(3), two of the three rate Eqs. (19)–(20) for the intracellular ion concentrations, and Eq. (27) for vascular K^+ regulation. All model parameters are listed in Table 1.

With our choice of dynamical variables, ion dynamics naturally decomposes into transmembrane ion changes and exchange with the external vascular reservoir. Transmembrane ion dynamics are given by Eqs. (18)–(20) and reservoir coupling by Eq. (27). We can see from the mass conservation constraints for K^+ that changes of K_e can be due to changes of K_i and ΔN^K, so both mechanisms are involved. Na_e and Cl_e only change by transmembrane fluxes.

The different processes come with distinct timescales which makes it possible to interpret the model dynamics in a slow–fast analysis (see below). Timescales can be derived from the model parameters (Hübel and Dahlem 2014) and are listed in Table 2.

Table 2 Timescales

Name	Value & unit	Description
τ_V	0.05 msec	potential changes
τ_n	1 msec	K^+ activation
τ_h	1 msec	Na^+ inactivation
τ_{Na}	0.5 sec	transm. Na^+ fluxes
τ_K	0.5 sec	transm. K^+ fluxes
τ_{Cl}	50 sec	transm. Cl^- fluxes
$\tau_{\Delta K}$	35 sec	K^+ gain/loss

To model temporary OGD, we set the maximal pump rate ρ and the diffusive coupling constant λ to zero. Both vascular coupling and transmembrane pumping are energy consuming processes that are interrupted or strongly weakened during OGD (Zandt et al. 2011; Wei et al. 2014a; Ullah et al. 2015). We analyze the response to OGD of systems with different ECS volumes. It is conventional to quantify this in terms of the extracellular volume fraction f_e. In modeling papers this quantity is often defined as the fraction of the ECS in a system that is composed of the neuron and the ECS only, and our normal ECS in Table 1 corresponds to a value of 25 %. Experimentally measured values normally relate the ECS volume to the whole tissue which includes the glia cells too. If we assume neurons and glia cells to make up approximately the same amount of volume, an ECS as in Table 1 corresponds to about 14 % of the whole tissue. All values of f_e given in this paper will refer to whole tissue including glia.

A computational study by Kager et al. (2000) on epileptic seizures and spreading depression uses an extracellular volume fraction of 15 % and refers to data of rat hippocampus (McBain et al. 1990; Mazel et al. 1998) suggesting values between 13 % to 20 %. Other studies report values ranging from 25 % in turtles (Krizaj et al. 1996) to 32 % in mice (Xie et al. 2013), and 27 % in human patients with focal cortical dysplasias (Zamecnik et al. 2012). The standard method in these measurements is real–time iontophoresis, a method in which the diffusion profile of externally applied cations is measured with electrodes at different points in the tissue. With this data the extracellular volume fraction and turtuosity can be derived from a radial diffusion equation. Neural densities are normally obtained by counting cells in small tissue volumes. While both measures are reported to be strongly brain region–dependent (Collins et al. 2010; McBain et al. 1990), there is to our knowledge no study or review giving a comprehensive overview of typical values for different regions. In this study we hypothesize differences in the extracellular volume fractions to be the cause for the observed brain region–dependent recovery behaviors from AD. We

therefore vary ω_e systematically with a starting value from Table 1 which is on the lower side of the measured range. However, this value is only used for one simulation example and we will discuss the effect of the ECS volume on the neural dynamics for a whole range of values up to almost 50 %.

We remark that it is irrelevant for our analysis if we increase f_e by increasing the ECS volume size, by decreasing the size of neural and glial compartment or by a combination of both. The only quantity that is dynamically relevant is the volume fraction f_e. In the program code we have varied ω_e and kept ω_i constant for simplicity. Accordingly our range of ω_e variation is rather large (up to more than 3,500 μm^2). This is an artifact of our way of parameter variation and the focus should rather be on the corresponding volume fractions. These are within or close to the normal physiological range.

Note that varying ω_e or f_e corresponds to different types of tissue, and it must not be confused with cell swelling as observed in ischemic edema (Lauderdale et al. 2015; Rosenberg 1999). Such osmosis–driven volume changes happen in AD, and they can be incorporated into the model without any problems (Ullah et al. 2015; Wei et al. 2014b). However, it can be shown that cell swelling is only a byproduct of the other processes that govern depolarization and recovery. Volume dynamics are not necessary to understand the interplay of mechanisms that leads to different recovery behaviors in different brain regions in AD. Ultimately neural damage will be due to cell swelling and also excitotoxicity, which relates to the dynamics of calcium and

neurotransmitters. So to understand the details of longterm neural damage such processes would have to be modeled. In this study, however, we focus on the initial processes that govern depolarization and recovery. For these events swelling will only alter the numerical values of critical parameters, but not the main course of events. That is why, it is not included and instead we discuss the fundamental phenomenon in a model that is as simple as possible. The effect of swelling on derived critical parameter values is briefly addressed in the discussion.

Simulation and bifurcation code is made available from ModelDB (Hines et al. 2004) with accession number 187213.
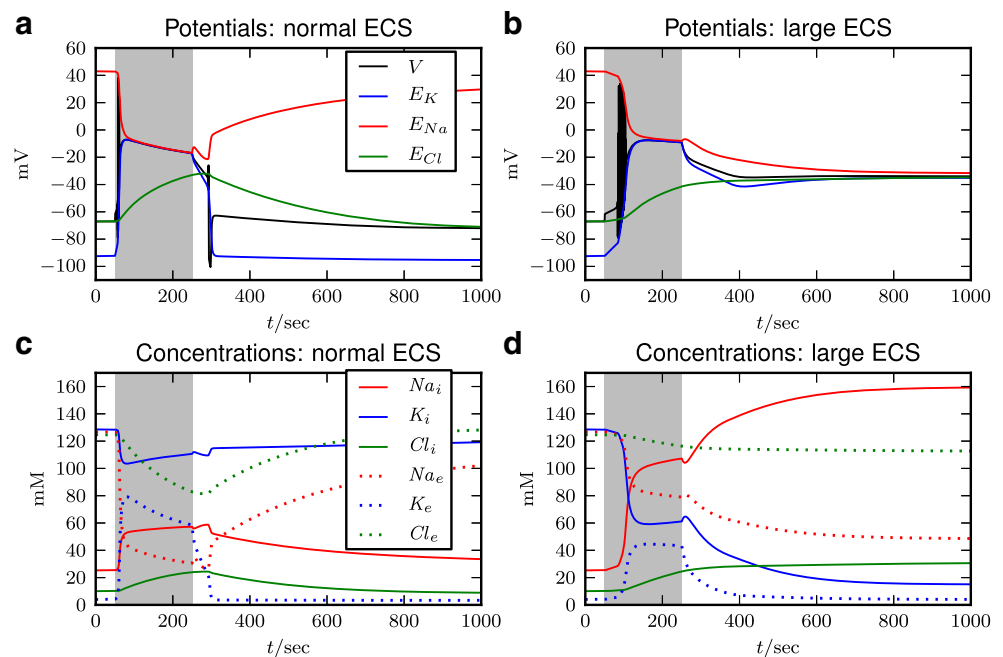
3 Results

3.1 Response of the model to OGD

We compare the response to 200 sec of OGD for a system with a normal ECS (14.3 %, 720 μm^3) and one with a large ECS (46.1 %, 3,700 μm^3). In the experiments by Brisson and Andrew (2012) and Brisson et al. (2013) the duration of OGD is longer and depolarization only sets in after some minutes of OGD. The pump activity gradually reduces with OGD and since this effect differs between brainstem and higher brain regions we see a delayed onset in the upper trace of Fig. 1.

This effect is well understood and hence for simplicity we do not model this transient onset behavior here. Instead

Fig. 3 Simulation of the neural response to 200 sec of OGD (shaded region). For the normal ECS, we use $f_e = 14.3$ % (with $\omega_e = 720$ μm^3), for the large ECS, we have $f_e = 46.1$ % (with $\omega_e = 3,700$ μm^3). The upper panels (a) and (b) show the evolution of the membrane and Nernst potentials. The lower panels (c) and (d) show the corresponding changes in ion concentrations. OGD leads to AD with reduced ion gradients and potential differences. The cell is recoverable from AD for the normal ECS and non–recoverable for the large ECS

pump activity and vascular coupling immediately drop to zero when OGD is applied and our focus is only on the recovery dynamics.

The result of the simulations is shown in Fig. 3. The upper panels (Fig. 3a and b) show the evolution of potentials for the two cases. The corresponding changes of ion concentrations are presented in the lower panels (Fig. 3c and d). The initial response to OGD is similar in both cases. The neuron quickly depolarizes and the Nernst potentials of K^+ and Na^+ get very close to the membrane potential. The Cl^- potential is driven to the same point, but changes more slowly. The most striking changes of ion concentrations are the extreme elevation and drop of extracellular K^+ and Na^+, respectively.

After OGD, pumps and vascular coupling are at work again and the system with the normal ECS recovers from the depolarized state (Fig. 3a and c). At first, the neuron is slowly repolarized until it reaches a point of abrupt hyperpolarization. The membrane potential drops even below E_K, because the K^+ channels close and the pump current overpowers I_K for a brief moment. The sharp potential drop is followed by the slow asymptotic return to the initial physiological resting state. Nernst potential differences and ion gradients are re–established. In contrast, the model with the large extracellular volume fraction does not recover (Fig. 3b and d). After a short phase of moderate repolarization, the membrane potential and Nernst potentials settle at a still strongly depolarized level, and most importantly, potential differences remain very small. Accordingly, ion concentrations are still extremely far from normal physiological conditions. Only the external K^+ concentration returns to its physiological resting value of 4 mM, because we assume an idealized regulation scheme for K^+.

We see that in both cases OGD induces AD, which is characterized by membrane depolarization and drastically reduced Nernst potential differences. For the normal ECS, the combined effort of ion pumps and vascular coupling brings the cell back to normal physiological conditions. For the larger ECS, the neuron does not recover from AD despite the presence of fully functional pumps and vasculature. This is a reproduction of the experimentally observed behavior in Fig. 1 and a similar result to Ullah et al. (2015). In the following sections we will investigate the nature of this recovery failure.

3.2 Recovery threshold and phase space analysis

Before proceeding to the threshold analysis, we need to review the basic phase space structure of neural ion dynamics. Ion exchange with the vascular system is a much slower process than transmembrane ion fluxes (see Table 2). This

gives rise to a recently developed slow–fast analysis of the dynamics in the system (Hübel and Dahlem 2014).

The idea behind the analysis is the following thought experiment. We imagine a neuron model without the external reservoirs, and instead of dynamical reservoir coupling we modify the overall K^+ content in the ICS and ECS by hand. Formally this is done by treating ΔN^K as a parameter rather than a dynamical variable and neglecting the rate equation for vascular coupling. This provides us with a useful perspective on the full model ion dynamics, since—as mentioned above—reservoir coupling is slow in comparison to membrane and transmembrane processes. Accordingly at every instant of time we expect the variables other than ΔN^K to behave as they would in a system where ΔN^K is fixed as a parameter.

To make use of this perspective quantitatively we vary ΔN^K to derive the fixed point structure of the transmembrane systems with different K^+ contents. For the dynamics of the full model we expect the fast variables of membrane and transmembrane dynamics to have enough time to settle near or to these fixed points. The phase space trajectory of the model is hence guided by this underlying fixed point structure. If this structure changes, the dynamics of the system changes accordingly.

Figure 4 illustrates how this works in the normal case. The black, s–shaped curve indicates where the fixed points
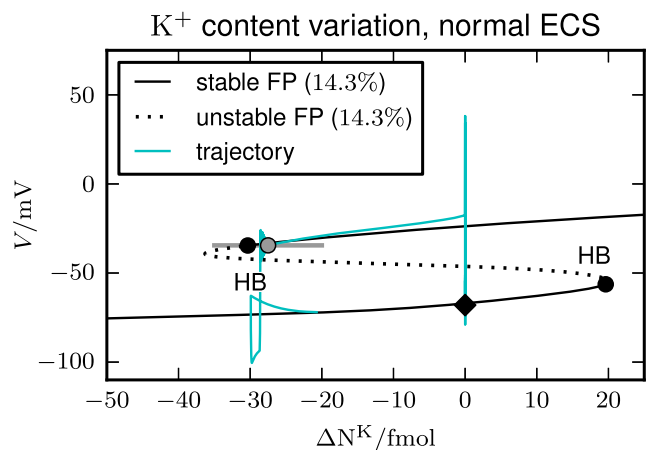

Fig. 4 Phase space plot for normal ECS (Fig. 3a and c). The black curve shows the fixed point (FP) structure of the fast model dynamics as a function of ΔN^K with fully functional pumps (i.e. normal oxygen–glucose supply). The stable branches (solid lines) become unstable in Hopf bifurcations (HB). The trajectory from Fig. 3a (turquoise curve) follows the stable branches. The grey line around the HB point indicates the threshold location for different values of Cl_i (higher values to the right). The system repolarizes at a higher Cl_i–value (grey bullet) than the one belonging to the HB of the exact transmembrane fixed point curve (black bullet)

of the fast dynamics, i.e. membrane dynamics and transmembrane ion fluxes, lie. We see that there are two stable states (black solid lines) for a wide range of ΔN^K–values. Conditions on the more polarized, stable branch are generally comparable to the initial physiological resting state that is marked by the black diamond. In particular, the differences between Nernst potentials are large (not shown in Fig. 4) and the neuron is capable of normal spiking activity, for example in response to synaptic input or background noise.

On the upper branch the situation is entirely different and the depolarized fixed points are in many aspects comparable to the thermodynamic Donnan equilibrium of the system. The Donnan equilibrium is attained when the system is completely isolated and there is neither particle exchange with its surroundings nor energy supply for the ion pumps. The membrane potential and all Nernst potentials are then at the same depolarized Donnan potential.

The points on the depolarized branch in Fig. 4 are stable and close to the Donnan equilibrium despite fully functional pumps. For neural function, however, the crucial point is only where spiking activity is possible. This requires a sufficient amount of electrical energy that is stored in the ion gradients such that potential differences are large. On the depolarized branch the amount of available electrical energy is too low for neural function and we refer to these dysfunctional conditions as free energy–starvation (FES). The physiological resting state, the Donnan equilibrium, and FES for $\Delta N^K = 0$ fmol are compared in Table 3.

The fixed point lines are obtained by the continuation software tool AUTO (Doedel and Oldeman 2009). Stability changes occur via bifurcations. The two generic cases are Hopf bifurcations (HB) and limit point bifurcations

Table 3 Physiological conditions, Donnan equilibrium and FES for $\Delta N^K = 0$ fmol

	Phys.	Donnan	FES	Units
V	−67.1	−22.6	−23.7	mV
n	0.065	0.636	0.622	1
m	0.065	0.681	0.657	1
h	0.065	0.075	0.085	1
Na_i	25.3	59.1	56.9	mM
Na_e	126.8	25.3	32.0	mM
K_i	128.6	113.7	115.4	mM
K_e	4.0	48.6	43.5	mM
Cl_i	10.1	29.0	28.5	mM
Cl_e	124.6	67.8	69.4	mM
E_{Na}	43.0	−22.6	−15.3	mV
E_K	−92.5	−22.6	−26.0	mV
E_{Cl}	−67.1	−22.6	−23.7	mV
I_p	0.63	0.00	6.8	$\mu A/cm^2$

(LP). We only indicate bifurcations to or from fully stable fixed points and omit those that only change the degree of instability.

Figure 4 provides the following interpretation of the neural response to OGD for the normal ECS (Fig. 3a and c). During OGD the physiological resting state becomes unstable and the system evolves towards its Donnan equilibrium. When OGD is over the cell is near the FES–branch and is hence attracted by it. K_e is significantly elevated and the vasculature starts taking up K^+. Accordingly the K^+ content decreases and the trajectory bends towards negative ΔN^K–values. The FES–branch guides the trajectory until it becomes unstable in a Hopf bifurcation, the cell repolarizes and ion gradients are rebuilt. The final return to the initial point is slow. Please note that we have added a grey line around the Hopf bifurcation point. It indicates the threshold location for different values of Cl_i (higher values to the right). This is necessary because Cl_i is similarly slow as ΔN^K (see timescales in Table 2) and the Cl^- concentrations cannot catch up with the changes of the K^+ content as quickly as the other variables. Hence Cl_i tends to remain slightly higher than its fixed point value.

A first insight why the response for a larger ECS is completely different is given in Fig. 5. The underlying fixed point structure has drastically changed. It differs from Fig. 4 in that the FES–branch remains stable. There is no recovery threshold even for an extreme reduction of the K^+ content. Accordingly, after OGD there is no point at which the membrane potential drops back to a normal physiological level. The cell does not recover from AD.

Figures 4 and 5 show that the existence of a recovery threshold crucially depends on the ECS volume size. In Fig. 5b the two FES–branches are compared. In addition, we follow the recovery point for a continuously increasing ECS volume, which yields the green Hopf line. It shows that the FES–branches end in Hopf bifurcations for extracellular volume fractions of up to 45 % (marked by a green star). At this critical volume fraction the recovery Hopf line vanishes in a fold–Hopf bifurcation with a second Hopf line (dashed green line). This formally proves that recovery is not possible for higher volumes. The threshold value is higher than the typical values around 20–30 % that we expect to find in living tissue (McBain et al. 1990; Mazel et al. 1998; Krizaj et al. 1996; Xie et al. 2013; Zamecnik et al. 2012). However, certain model refinements can shift the critical volume fraction well into this physiological range (see discussion). It has been shown theoretically that recovery from FES is due to external K^+ uptake and cannot be accomplished by the ion pumps alone (Hübel et al. 2014). This is also confirmed by the inset in Fig. 5b, which shows the fixed point structure for pump strength variation for both normal and large ECS
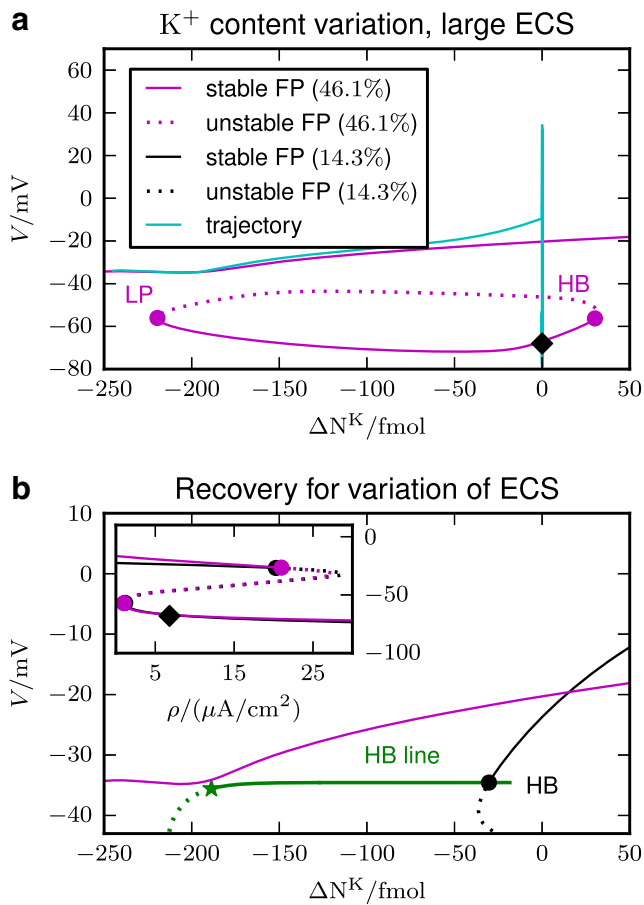
Fig. 5 Phase space plot for large ECS and comparison with normal ECS case. Panel (**a**) shows a phase space plot for OGD and a large ECS (Fig. 3b and d). The pink curve indicates the underlying FP structure at fully functional pumps (i.e. normal oxygen–glucose supply). The FES branch does not become unstable for low values of ΔN^K. The trajectory remains on the FES–branch. Panel (**b**) shows the FES–branch for both cases and the location of the recovery point for all extracellular volume fractions f_e between 10 % at the right end of the Hopf (HB) line and 45 % at the left end (marked by the star). The dashed HB line indicates second Hopf bifurcations for ECS volumes less than 45 %. At higher volumes no more Hopf bifurcations occur. The inset shows the fixed point as the maximum pump strength is varied. The diamond marks normal physiological conditions

volumes and $\Delta N^K = 0$. On the depolarized branches, the sigmoidal pump function of Eq. (21) is saturated and the current I_p is about five times stronger than on the physiological branches. The normal resting state with maximal (but not saturated) pump strength $\rho = 6.8 \ \mu A/cm^2$ is again marked by a black diamond. In both cases, the depolarized branch becomes unstable only for very large pump rates ($\rho > 21 \ \mu A/cm^2$). This threshold is almost independent of the ECS volume, and it corresponds to a pump current that is more than 15 times higher than during normal physiological conditions. Although different isoforms of Na^+/K^+ exchange pumps in different areas of the brain

have been reported (Blanco 2005; Dobretsov and Stimers 2005), we are unaware of such big region–specific differences in the pump activity. That is why we focus on how ΔN^K facilitates recovery from FES in this study. However, the differences in the function of different isoforms of Na^+/K^+ exchange pumps are more complicated than just changing the maximum pump strength as done in the inset in Fig. 5a of this paper and in Hübel et al. (2014). Thus, we leave the investigation of whether different pump isoforms could lead to cell's recovery from AD for the future. This point is highlighted further in the Discussion section.

3.3 Why recovery fails for a large ECS

Up to this point we have only reproduced the two types of neural response to OGD from Fig. 1, and we have seen that the dynamics is consistent with a change of the underlying fixed point structure as shown in Fig. 5b. The major advantage of the phase space perspective that we here provide is that we can track the recovery point for all extracellular volume fractions f_e from 10 % up to 45 %, where recovery fails. This threshold analysis will help us understand why the model has a critical volume fraction beyond which recovery becomes impossible. We have included the threshold Hopf line already in Fig. 5b, but only the membrane potential is shown and also the dependence on f_e is not explicit.

More detailed information on the system conditions at the recovery threshold for different ECS volumes is given in Fig. 6. Generally, for each extracellular volume fraction for which recovery is possible, the cell slowly repolarizes—coming from deep FES—until the recovery point is reached (see the example in Fig. 4). The Nernst potentials E_K and E_{Na}, and the extracellular concentrations K_e and Na_e decrease as the system evolves towards this point.

The first thing to note is that increasing the extracellular volume fraction fraction goes along with shifts of the threshold ion concentrations (Fig. 6a). The potentials remain at almost exactly the same levels (Fig. 6b). The observed ion shifts in Fig. 6a are indeed a consequence of the constant threshold potentials. To see this let us for now assume that recovery happens at certain levels of Nernst potentials that are—as Fig. 6b suggests—independent of the ECS volume size. If this is the case then recovery is about reaching the threshold values of the ion concentration fractions

$$\chi_{Na}^* = \frac{Na_e^*}{Na_i^*} = 0.448 \,,$$

$$\chi_K^* = \frac{K_e^*}{K_i^*} = 0.210 \,,$$

that belong to these potentials. So we simply translate what Fig. 6b shows into the following equivalent statement:
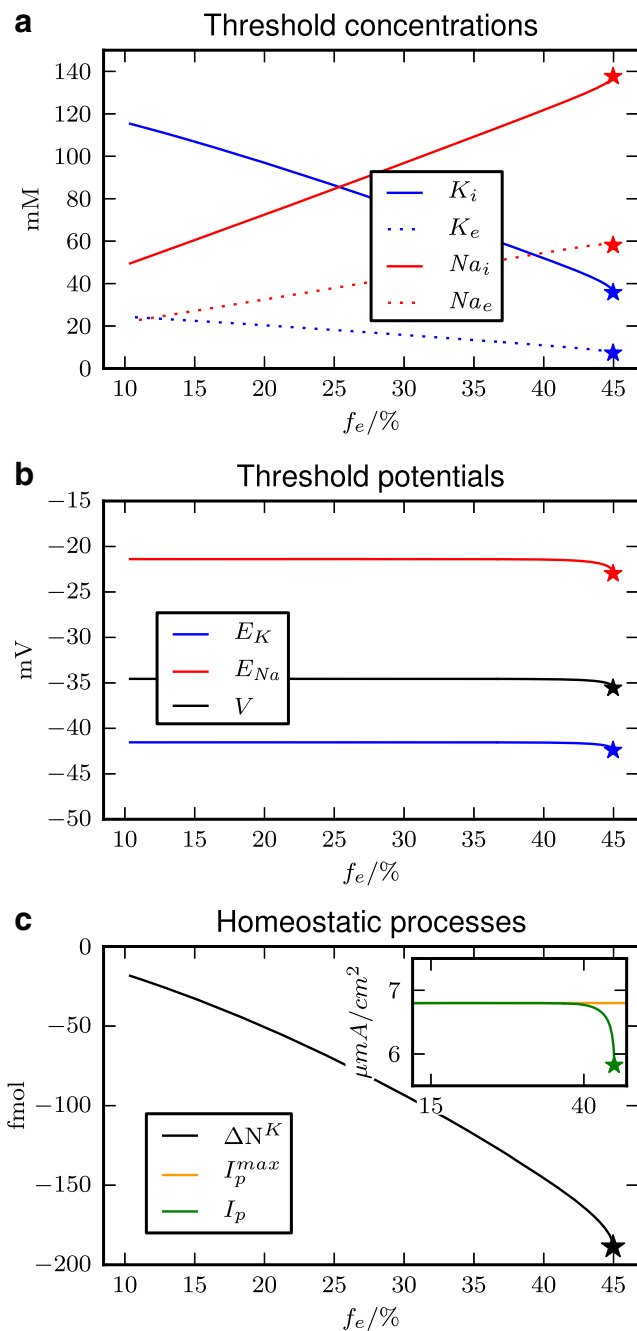
Fig. 6 Values of dynamical variables and other quantities at the recovery threshold obtained from the Hopf line continuation (green line in Fig. 5b). The extracellular volume fraction f_e is varied from 10 % up to recovery failure at 45 % (marked by stars in each panel). Panels **(a)** and **(b)** show ion concentrations and threshold potentials respectively. The main part of panel **(c)** shows how much K^+–uptake is needed to reach the recovery point. The inset shows the pump activity at the threshold. The maximal pump level (which is identical to ρ) is indicated by the orange line

For every extracellular volume fraction f_e between 10 % and almost 45 % the two above conditions define the repolarization point.

For our following argument it is not important how exactly the neuron depolarizes and how the homeostatic mechanisms take it to this repolarization point. We simply need to understand that all these processes result in a redistribution of ions compared to the initial resting state which is given in the first column of Table 3 and is denoted by a superscript 0 in the following. In our model these resting ion concentrations are the same for each choice of f_e. At these initial concentrations we have $\chi_{Na}^0 = 5.012$. So the threshold concentration Na_e^* must be lower than Na_e^0—regardless of the volume fraction f_e. However, how much lower Na_e^* has to be will depend on the ECS volume.

To see this let us consider a system with a normal ECS first. For this system to be at the recovery point, more Na^+ ions must be inside the cell and accordingly fewer in the ECS than initially. So let there be a redistribution of Na^+ ions such that the system with the normal ECS is at threshold and $\chi_{Na}^{(norm)} = \chi_{Na}^*$. For a clear distinction between the situation with a normal and a large ECS we add superscripts *(norm)* and *(large)*. In a system with a large ECS that same redistribution will be insufficient. While the intracellular concentrations $Na_i^{(norm)}$ and $Na_i^{(large)}$ will have the same increased value, the redistribution does not reduce the extracellular Na^+ concentration as much, i.e. $Na_e^{(large)} > Na_e^{(norm)}$, simply because the ECS is larger. Consequently $\chi_{Na}^{(large)}$ will not be small enough and more Na^+ in the ICS is needed. This way the condition $\chi_{Na}^{(large)} = \chi_{Na}^*$ will be satisfied by two higher concentrations:

$$Na_i^{*(large)} > Na_i^{*(norm)} ,$$
$$Na_e^{*(large)} > Na_e^{*(norm)} .$$

By electroneutrality, a higher concentration of Na^+ in the ICS implies a lower concentration of K^+, i.e. $K_i^{*(large)} < K_i^{*(norm)}$. Then the condition $\chi_K^{(large)} = \chi_K^*$ implies that $K_e^{*(large)}$ must also be smaller:

$$K_i^{*(large)} < K_i^{*(norm)}$$
$$\chi_K^{(norm)} = \frac{K_e^{*(norm)}}{K_i^{*(norm)}} = \chi_K^*$$
$$\chi_K^{(large)} = \frac{K_e^{*(large)}}{K_i^{*(large)}} = \chi_K^*$$
$$\Rightarrow \quad K_e^{*(large)} < K_e^{*(norm)}$$

This simple effect that a larger ECS volume has is the key to understand the change of the phase space. Most importantly we see that FES in a system with a large ECS tolerates lower extracellular K^+ concentrations. This affects both homeostatic mechanisms, the ion pumps and vascular K^+–uptake. Figure 6c shows that the decreasing K_e level at the threshold goes along with a higher K^+–uptake demand. This is reflected in more negative ΔN^K–values for larger ECSs.
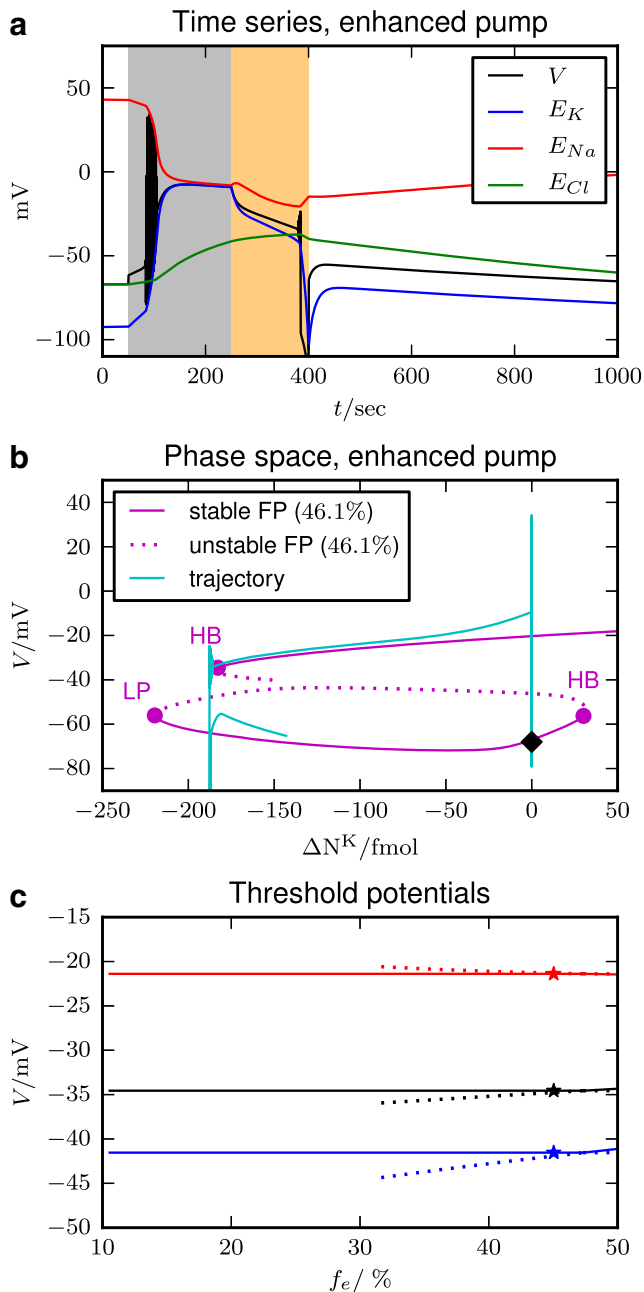
Fig. 7 Simulations and thresholds for non–physiological, enhanced pump activity and a large ECS. Panel **(a)** shows the response to OGD (gray shaded region). After OGD the pump activity is kept at the maximum level until the cell repolarizes (orange shaded region). The cell recovers. Panel **(b)** gives the phase space picture. Along the FES–branch a maximal pump activity that is independent of ion concentrations is assumed. FES becomes unstable in a Hopf bifurcation (HB) and the trajectory returns to the physiological branch. In panel **(c)** are threshold potentials for a continuous variation of ω_e under the assumption that the pump activity is maximal. Recovery is possible far beyond the former critical value (star markers). Potentials at second bifurcations are presented by the dashed lines

Our diffusive coupling scheme has an unlimited uptake capacity, but in a physiologically more detailed description this high uptake demand could lead to recovery failure.

In our model, however, recovery failure must be explained differently.

We should instead direct our attention to the inset of Fig. 6c. It shows the magnitude of the pump current at the threshold, and we see that it is maximal almost for the entire range of ECS volumes. When recovery fails, however, it drops significantly. This is because K_e decreases and the pump function I_p from Eq. (21) is no longer saturated. Exchange of intracellular Na^+ for extracellular K^+ happens no longer at the maximal turnover rate, because the concentration of K^+ in the ECS is already rather low.

In summary, Fig. 6 shows that recovery from FES happens at certain values of the Nernst potentials and at maximal ion pumping for almost all ECS volumes up to the critical value $f_e = 45\%$ beyond which recovery becomes impossible. Near this critical volume fraction both, the Nernst potentials and the pump current are no longer constant (with respect to f_e). However, the relative changes of Nernst potentials are clearly less pronounced than the drop of the pump current, and we hence assert that recovery failure is due to insufficient pump activity.

We formally prove this hypothesis by demonstrating that enhanced ion pumps would prevent recovery failure. This is shown in Fig. 7. For the simulation in Fig. 7a and b, we apply the same OGD protocol as before to a cell with a large ECS. However, after OGD we keep the pump activity at the maximum level until the neuron repolarizes (orange shaded region). The plot shows that with this modification recovery is possible. The fixed point structure in Fig. 7b changes accordingly and the FES–branch ends in a Hopf bifurcation. Note that for the fixed point structure, we have assumed the enhanced pump only along the FES–branch.

A threshold continuation as in Fig. 6b yields the threshold potentials in Fig. 7c. This diagram shows that recovery would always be possible if the pump activity would not decrease with K_e. The former point of recovery failure is still marked by a star, but the recovery line extends beyond this point up to $f_e = 50\%$ and higher. The diagram also contains the potentials of a second bifurcation (dashed lines) that takes over at $f_e = 47.3\%$, but such details are not relevant to our discussion. Fig. 7 mainly illustrates that a decrease in pump activity is the reason for recovery failure. This renders the region–specific differences in pump activity contributing to the AD recovery failure as a critical question for future investigations.

3.4 Recovery as switching of the membrane state

Our above discussion of recovery failure has implicitly relied on the assumption that the recovery point is characterized by the Nernst potentials and the pump activity. While ion concentrations at threshold vary a lot between models with different ECSs, the values of Nernst potentials

and pump current are constant almost up to the critical volume. This naturally led us to assume and indeed confirm that recovery fails because pumping gets weaker.

The pump current I_p and the Nernst potentials E_{ion} fully determine the membrane dynamics. So for all values of f_e between 10 % and almost 45 %, the membrane dynamics at the repolarization point are the same. In other words, it seems like recovery comes down to one specific process in the membrane.

To see if this is really the case, we analyze the membrane state around the recovery point separately for the normal ECS. We therefore treat the Nernst potentials as system parameters and vary them such that the values are as on the FES–branch. The normally very slowly changing Cl^- concentrations are kept fixed at the values at threshold. This variation is naturally parametrized by ΔN^K. Only now ΔN^K indicates how the parameters E_{ion} are varied, and not where the dynamical quantities E_{ion} have a fixed point. The only dynamical variables in this adapted variation of Nernst potentials are V, n and h. The pump current is kept at maximum.

The result in Fig. 8 is as expected. The inset indicates how the Nernst potentials are simultaneously varied. The main part shows the fixed points of the separated HH dynamics. There are two stable branches for $\Delta N^K > -27.6$ fmol. The depolarized branch guides the trajectory

(turquoise curve) until it destabilizes in a Hopf bifurcation. The lower, polarized branch is only a fixed point of the membrane dynamics. On this branch the membrane potential is stable because the sum of all currents vanishes. However, the current terms $(I_{K^+} - 2I_p)$ and $(I_{Na^+} + 3I_p)$ governing the ion fluxes do not vanish individually. Therefore the V–values on the lower branch are not compatible with stable ion concentrations and the repolarization drop to this branch is only the initial process, after which ion concentrations adjust themselves and ion gradients are rebuilt. The trajectory then approaches the fixed point of membrane dynamics and transmembrane ion dynamics as in Fig. 4.

The Hopf bifurcation in this separated HH system lies exactly where the larger system of transmembrane ion dynamics bifurcates (compare Fig. 8 main with Fig. 4). Conversely, we can consider the other subsystem for which the membrane potential V and gating variables n and h are varied as parameters and only ion concentrations are modeled (not shown). This model of separated ion dynamics remains stable at $\Delta N^K = -27.6$ fmol. This proves that the fundamental process at the repolarization point is a switching of the membrane potential according to the bifurcation scenario of Fig. 8.

4 Discussion

Computational modeling has the potential to deepen our understanding of real physical processes. In a modeling approach we can separate mechanisms that cannot be separated in an experimental setup. Ideally this leads to novel insights that go beyond current experimental results.

In neuroscience, because of the extreme complexity of the real physical system, every mathematical model will typically have to focus on a specific aspect of neural behavior. AD is a pathological process that goes along with the breakdown of ion gradients and the complete cessation of neural electrical activity. It has been shown experimentally and in other computational studies that for such extreme processes, the biophysical details of the ion channels and their gating dynamics play a minor role (Mulet and Mirasso 1999; Kager et al. 2000; Hübel et al. 2014; Hübel and Dahlem 2014; Wei et al. 2014b). A simple HH set of ion channels and gating variables is sufficient to describe neural ion dynamics on a fundamental level.

Specifically, two processes left out in our model are calcium dynamics and dynamic cell swelling. Both do not change the phase space perspective we have presented above. The role of calcium–induced glutamate release and NMDA and AMPA receptor gating can be incorporated, but would only be a minor modification of the gating dynamics.
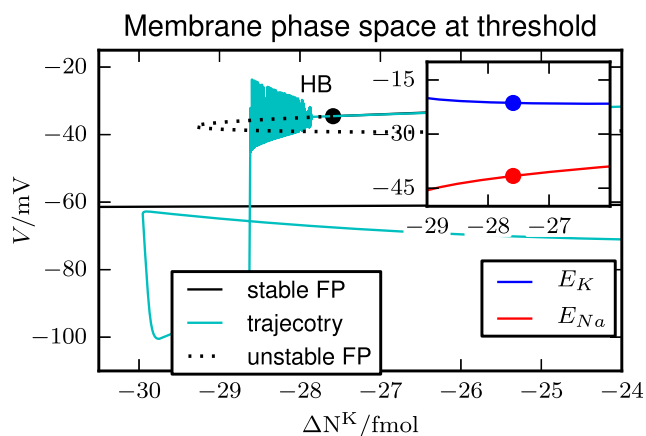

Fig. 8 Phase space of membrane dynamics. Nernst potentials are varied simultaneously such that values are like on the FES–branch in Fig. 4. The variation is parametrized by ΔN^K as shown in the inset. There are two fixed point branches. The depolarized branch becomes unstable in a Hopf bifurcation (HB). The more polarized branch is stable for the full parameter range. The upper branch guides the trajectory. Repolarization is onto the lower branch. Then processes beyond pure membrane dynamics govern the further course of the trajectory

The direct effect of calcium currents is negligible in comparison to K^+ and Na^+ in our model. However, a model for neurotransmitter release and synaptic communication should take calcium dynamics into account. Also dynamical cell swelling will modify the model dynamics quantitatively, but will preserve the phenomenon and the general argument presented here.

This is not to say that biophysical detail is unimportant. Specific threshold values and parameter ranges of different neural behaviors will depend on all model components, and a quantitative assessment of these dependencies is beyond the scope of this study. What we claim, however, is that the simplified approach we chose here uncovers some general connections between the homeostatic mechanisms and the cell morphology. While the value of the critical ECS volume size may be different in real nervous tissue, our explanation for recovery failure is very general and will apply in every more detailed model.

The subject of this study is to explain the observations about the ischemia–induced AD, namely that there is a clear connection between the brain region and the resistance of the cell to recover from AD (Brisson and Andrew 2012; Brisson et al. 2013). Non–recoverable AD is the physiological process behind brain damage due to ischemia caused by heart attack, near drowning, or traumatic brain injury. In a related computational study, we suggested that the tissue–dependent extracellular volume size could be a potential cause for different extents of AD (Ullah et al. 2015). Here, we systematically analyze how the recoverability depends on the ECS and elucidate the mechanisms that lead to the the cell's failure to recover from AD.

For a small ECS, which corresponds to hypothalamic tissue in our model, AD is recoverable, while for a large ECS corresponding to model equivalent of neocortex or thalamic tissue, the depolarization is permanent. This is consistent with the experimental data in Fig. 1. To investigate the transition between these behaviors, we applied a recently developed slow–fast decomposition that separates transmembrane ion fluxes from vascular coupling. The recovery point then becomes a bifurcation of the transmembrane ion dynamics, and tracking this bifurcation shows that it disappears for a critical ECS volume size. For a larger ECS, the neuron cannot recover and the failure is hence abrupt rather than gradual. Our model is thus consistent with experimental data which shows that the thalamus–hypothalamus interface is the distinct boundary between recoverable and non–recoverable AD (Brisson et al. 2013).

Our slow–fast decomposition of ion dynamics suggests a hierarchy of the homeostatic mechanisms during recovery from AD. The most important process is K^+ diffusion into the vasculature uptake. Vascular coupling reduces the K^+ concentration in the ECS until the repolarization point is reached. We show that for a larger ECS, this point lies at a more negative value and thus more K^+–uptake is required. While the uptake capacity of our model is unlimited, in a real system this higher demand may cause recovery failure in the higher brain regions.

Another key point is that a low extracellular K^+ concentration slows down the transmembrane Na^+/K^+–exchange. While vascular K^+–uptake is needed to reach the repolarization point, the recovery process itself is mainly driven by the ion pumps (Figs. 5 and 7). If these are too weak, recovery fails regardless of the uptake capacity of the vasculature. The conclusion that Na^+/K^+–ATPase does not function at its full capacity in the upper brain regions is in line with the hypothesis put forward by Brisson and Andrew (2012) and Brisson et al. (2013) based on the their observations. The authors hypothesized that the difference in pumps' activity leading to the different AD strength and recovery in response to temporary OGD or ouabain (Na^+/K^+ pump blocker) application could be due to the different pump isoforms in the upper and lower brain regions. Our results show that even with the same maximum capacity (isoform), the pumps in the higher brain regions do not function up to their full capacity due to the lower extracellular K^+ concentration. This result in the AD recovery failure. The explanation is independent of the question how different pump isoforms may alter the course of AD. The effect of the latter can only be addressed in more detailed pump model that accounts for such differences between the brain brain regions. While for this study we have exclusively focused on the role of the extracellular volume fraction, the question of pump isoforms is clearly a future challenge.

Our model predicts that for Na^+/K^+ATPase to lead to cell's recovery from AD, the pumps would have to function at a rate 15 times higher during ischemia than the physiological value (Fig. 5b). Although this kind of variability seems very high, we cannot rule out the possibility of different brain region-specific pump isoforms (Blanco 2005; Dobretsov and Stimers 2005) leading to AD recovery either by itself or in some combination with other processes such as vascular clearance or differential ECS. Our preliminary data shows that higher brain regions strongly express the vulnerable $1\alpha1$ while lower brain regions express a higher proportion of the ischemia-efficient $1\alpha3$ isoform (unpublished results). The $1\alpha1$ isoform has steep voltage dependence in cortical neurons, so it quickly activates after short action potential bursts. In contrast, $1\alpha3$ activation is independent of voltage and displays low Na^+ and high ATP affinity, so it can continue functioning during prolonged depolarization (Dobretsov and Stimers 2005). The differential voltage dependence and ATP, Na^+, and K^+ (Dobretsov

and Stimers 2005) affinities make the theoretical representation of different pump isoforms more complex than simply using different maximum pump rates as represented in our model (see inset of Fig. 5b). Thus, a comprehensive model for Na^+/K^+–ATPase is required to fully understand the extent to which pumps play a role in the cell's recovery from AD. Na^+/K^+ pumps on glial and endothelial cells play a major role in vascular uptake. The $1\alpha2$ isoform is glial and is similarly ischemia–efficient as the $1\alpha3$ isoform. Hence a related question would be, if the $1\alpha2$ isoform exists in glial and endothelial cells in lower brain region where it would lead to efficient vascular uptake, which would partner with more potent neuronal pumps to result in the cell's recovery from AD.

We remark that the general phenomenon, i.e. an increased K^+–uptake demand for a larger ECS and recovery failure above a certain threshold, occurs in different model variants that we have tested. For example, a different set of initial conditions and pump rates may shift the threshold, but does not alter the results qualitatively. Our critical f_e–value for recovery failure in Fig. 6 is at 45 % which is rather high. One may hence conclude that the phenomenon should not be seen in real tissue. However, it turns out that including dynamical cell swelling lowers this threshold significantly. Also an electroneutral description of the vascular unit by the inclusion of anion channels reduces the threshold markedly. In such more realistic models, the critical ECS volume where recovery fails is as low as 23 %.

For future applications of our theory like the quantitative interpretation of real experimental data, a detailed analysis of these threshold dependencies will become important. At this point, however, we merely want to point out that the phenomenon as such is very robust and that volume fraction–wise the critical values can indeed be expected to lie in a physiologically realistic range.

Part of our results go beyond understanding the different recovery behaviors in AD. From a modeling perspective, SD is very similar to recoverable AD, which has also been pointed out in the experiments (Brisson et al. 2013) where the authors call SD a "milder AD–like event". Several studies suggest that recovery in SD is mostly accomplished by vascular coupling. The recovery failure scenario which we have analyzed here provides us with a more differentiated picture in which recovery is a combined effort of the Na^+/K^+–exchange pumps and the vasculature. We could furthermore show that recovery from AD is fundamentally due to one specific switching process in the neural membrane.

It will be a future challenge to develop new neuroprotective strategies based on our results. While the extracellular volume fraction cannot be changed easily, our simulation in Fig. 7a suggests that enhancing the ion pump turnover rate temporarily can be a way to support recovery. Certain adrenergetic agonists and antagonists that stimulate the Na^+/K^+ pumps are known and may be of help in these types of pathologies (Berthon et al. 1983; Sawas and Gilbert 1981). From a more general perspective this study should add to our understanding of risk factors for neural damage.

References

Attwell, D., & Laughlin, S.B. (2001). An energy budget for signaling in the grey matter of the brain. *Journal of Cerebral Blood Flow & Metabolism*, *21*(10), 1133–1145.

Barreto, E., & Cressman, J.R. (2010). Ion concentration dynamics as a mechanism for neural bursting. *Journal of Biological Physics*, *37*(3), 361–373. doi:10.1007/s10867-010-9212-6.

Bazhenov, M., Timofeev, I., Steriade, M., & Sejnowski, T.J. (2004). Potassium model for slow (2–3 Hz) *in vivo* neocortical paroxysmal oscillations. *Journal of Neurophysiology*, *92*, 1116–1132.

Berthon, B., Burgess, G.M., Capiod, T., Claret, M., & Poggioli, J. (1983). Mechanism of action of noradrenaline on the sodium–potassium pump in isolated rat liver cells. *Journal of Physiology*, *341*, 25–40.

Blanco, G. (2005). Na,k–ATPase subunit heterogeneity as a mechanism for tissue-specific ion regulation. In *Seminars in nephrology, vol. 25, pp. 292–303*: Elsevier.

Brisson, C.D., & Andrew, R.D. (2012). A neuronal population in hypothalamus that dramatically resists acute ischemic injury compared to neocortex. *Journal of Neurophysiology*, *108*(2), 419–430.

Brisson, C.D., Hsieh, Y.T., Kim, D., Jin, A.Y., & Andrew, R.D. (2014). Brainstem neurons survive the identical ischemic stress that kills higher neurons: insight to the persistent vegetative state. *PloS one*, *9*(5).

Brisson, C.D., Lukewich, M.K., & Andrew, R.D. (2013). A distinct boundary between the higher brains susceptibility to ischemia and the lower brains resistance. *PLoS ONE*, *8*(11), e79,589. doi:10.1371/journal.pone.0079589.

Centonze, D., Marfia, G., Pisani, A., Picconi, B., Giacomini, P., Bernardi, G., & Calabresi, P. (2001). Ionic mechanisms underlying differential vulnerability to ischemia in striatal neurons. *Progress in neurobiology*, *63*(6), 687–696.

Collins, C.E., Airey, D.C., Young, N.A., Leitch, D.B., & Kaas, J.H. (2010). Neuron densities vary across and within cortical areas in primates. *Proceedings of the National Academy of Sciences*, *107*(36), 15,927–15,932.

Cressman Jr., J.R., Ullah, G., Ziburkus, J., Schiff, S.J., & Barreto, E. (2009). The influence of sodium and potassium dynamics on excitability, seizures, and the stability of persistent states: I. single neuron dynamics. *Journal of Computational Neuroscience*, *26*, 159–170.

Cressman Jr., J.R., Ullah, G., Ziburkus, J., Schiff, S.J., & Barreto, E. (2011). Erratum to: The influence of sodium and potassium dynamics on excitability, seizures, and the stability of persistent states: I. single neuron dynamics. *Journal of Computational Neuroscience*, *30*, 781.

Dahlem, M.A., Schumacher, J., & Hübel, N. (2014). Linking a genetic defect in migraine to spreading depression in a computational model. *PeerJ*, *2*, e379. doi:10.7717/peerj.379.

Dijkhuizen, R.M., Beekwilder, J.P., van der Worp, H.B., van der Sprenkel, J.W.B., Tulleken, K.A., & Nicolay, K. (1999). Correlation between tissue depolarizations and damage in focal ischemic rat brain. *Brain research*, *840*(1), 194–205.

Dobretsov, M., & Stimers, J.R. (2005). Neuronal function and alpha3 isoform of the na/k–ATPase. *Frontiers in Bioscience*, *10*, 2373–2396.

Doedel, E.J., & Oldeman, B.E. (2009). *Auto-07p: Continuation and bifurcation software for ordinary differential equations*. Montreal: Concordia University.

Falini, A., Barkovich, A., Calabrese, G., Origgi, D., Triulzi, F., & Scotti, G. (1998). Progressive brain failure after diffuse hypoxic ischemic brain injury: a serial MR and proton MR spectroscopic study. *American Journal of Neuroradiology*, *19*(4), 648–652.

Fröhlich, F., & Bazhenov, M. (2006). Coexistence of tonic firing and bursting in cortical neurons. *Physical Review E*, *74*(031922).

Hansen, A.J., & Zeuthen, T. (1981). Extracellular ion concentrations during spreading depression and ischemia in the rat brain cortex. *Acta physiologica Scandinavica*, *113*(4), 437–445.

Herculano-Houzel, S., & Lent, R. (2005). Isotropic fractionator: a simple, rapid method for the quantification of total cell and neuron numbers in the brain. *The Journal of neuroscience*, *25*(10), 2518–2521.

Hines, M.L., Morse, T., Migliore, M., Carnevale, N.T., & Shepherd, G.M. (2004). ModelDB: a database to support computational neuroscience. *Journal of computational neuroscience*, *17*(1), 7–11.

Hodgkin, A.L. (1948). The local electric changes associated with repetitive action in a medullated axon. *Journal of Physiology*, *107*, 165.

Hodgkin, A.L., & Huxley, A.F. (1952a). The components of membrane conductance in the giant axon of Loligo. *Journal of Physiology*, *116*, 473–496.

Hodgkin, A.L., & Huxley, A.F. (1952b). Currents carried by sodium and potassium ions through the membrane of the giant axon of Loligo. *Journal of Physiology*, *116*, 449–472.

Hodgkin, A.L., & Huxley, A.F. (1952c). A quantitative description of membrane current and its application to conduction and excitation in nerve. *Journal of Physiology*, *117*, 500–544.

Hodgkin, A.L., Huxley, A.F., & Katz, B. (1952). Measurement of current–voltage relations in the membrane of the giant axon of Loligo. *Journal of Physiology*, *116*, 424–448.

Hoffmann, U., Sukhotinsky, I., Atalay, Y.B., Eikermann-Haerter, K., & Ayata, C. (2012). Increased glucose availability does not restore prolonged spreading depression durations in hypotensive rats without brain injury. *Experimental Neurology*, *238*(2), 130–132.

Hübel, N., & Dahlem, M.A. (2014). Dynamics from seconds to hours in Hodgkin–Huxley model with time–dependent ion concentrations and buffer reservoirs. *PLoS Comparative Biology*, *10*, e1003,941. doi:10.1371/journal.pcbi.1003941.

Hübel, N., Schöll, E., & Dahlem, M.A. (2014). Bistable dynamics underlying excitability of ion homeostasis in neuron models. *PLoS Comparative Biology*, *10*, e1003,551. 10.1371/journal.pcbi.1003551.

Ingram, J., Zhang, C., Cressman, J.R., Hazra, A., Wei, Y., Koo, Y.E., Žiburkus, J., Kopelman, R., Xu, J., & Schiff, S.J. (2014). Oxygen and seizure dynamics: i. experiments. *Journal of neurophysiology*, *112*(2), 205–212.

Kager, H., Wadman, W.J., & Somjen, G.G. (2000). Simulated seizures and spreading depression in a neuron model incorporating interstitial space and ion concentrations. *Journal of Neurophysiology*, *84*, 495–512.

Kager, H., Wadman, W.J., & Somjen, G.G. (2002). Conditions for the triggering of spreading depression studied with computer simulations. *Journal of Neurophysiology*, *88*(5), 2700.

Kager, H., Wadman, W.J., & Somjen, G.G. (2007). Seizure–like afterdischarges simulated in a model neuron. *Journal of Computational Neuroscience*, *22*, 105–128.

Krishnan, G.P., & Bazhenov, M. (2011). Ionic dynamics mediate spontaneous termination of seizures and postictal depression state. *The Journal of Neuroscience*, *31*(24), 8870–8882.

Krizaj, D., Rice, M.E., Wardle, R.A., & Nicholson, C. (1996). Water compartmentalization and extracellular tortuosity after osmotic changes in cerebellum of Trachemys scripta. *Journal of Physiology*, *42*(3), 887–896.

Lauderdale, K., Murphy, T., Tung, T., Davila, D., Binder, D.K., & Fiacco, T.A. (2015). Osmotic edema rapidly increases neuronal excitability through activation of NMDA receptor–dependent slow inward currents in juvenile and adult hippocampus. *ASN Neuro*, *7*(5), 1759091415605,115. doi:10.1177/1759091415605115.

Luigetti, M., Goldsberry, G.T., & Cianfoni, A. (2012). Brain mri in global hypoxia–ischemia: a map of selective vulnerability. *Acta Neurologica Belgica*, *112*(1), 105–107.

Mazel, T., Simonov, Z., & Sykov, E. (1998). Diffusion heterogeneity and anisotropy in rat hippocampus. *Neuroreport*, *9*(7), 1299–1304.

McBain, C.J., Traynelis, S.F., & Dingledine, R. (1990). Regional variation of extracellular space in the hippocampus. *Science*, *249*(4969), 674–677.

Mulet, J., & Mirasso, C.R. (1999). Numerical statistics of power dropouts based on the Lang-Kobayashi model. *Physical Review E*, *59*(5), 5400–5405. doi:10.1103/physreve.59.5400.

Murphy, T.H., Li, P., Betts, K., & Liu, R. (2008). Two-photon imaging of stroke onset in vivo reveals that nmda-receptor independent ischemic depolarization is the major cause of rapid reversible damage to dendrites and spines. *The Journal of Neuroscience*, *28*(7), 1756–1772.

Rosenberg, G.A. (1999). Ischemic brain edema. *Progress in Cardiovascular Diseases*, *42*(3), 209–216.

Sawas, A.H., & Gilbert, J.C. (1981). Effects of adrenergic agonists and antagonists and of the catechol nucleus on the Na^+, K^+–ATPase and Mg^2+–ATPase activities of synaptosomes. *Biochemical Pharmacology*, *30*(13), 1799–803.

Schüz, A., & Palm, G. (1989). Density of neurons and synapses in the cerebral cortex of the mouse. *Journal of Comparative Neurology*, *286*(4), 442–455.

Shandilya, S.G., & Timme, M. (2011). Inferring network topology from complex dynamics. *New Journal of Physical*, *13*(1), 013,004.

Somjen, G.G. (2004). *Ions in the brain: normal function, seizures, and stroke*. USA: Oxford University Press.

Sukhotinsky, I., Yaseen, M.A., Sakadžić, S., Ruvinskaya, S., Sims, J.R., Boas, D.A., Moskowitz, M.A., & Ayata, C. (2010). Perfusion pressure–dependent recovery of cortical spreading depression is independent of tissue oxygenation over a wide physiologic range. *Journal of Cerebral Blood Flow and Metabolism*, *30*(6), 1168–1177. doi:10.1038/jcbfm.2009.285.

Ullah, G., & Schiff, S.J. (2009). Tracking and control of neuronal hodgkin-huxley dynamics. *Physical Review E*, *79*(4), 040,901. doi:10.1103/physreve.79.040901.

Ullah, G., & Schiff, S.J. (2010). Assimilating seizure dynamics. *PLoS Comput Biol*, *6*(5), e1000,776.

Ullah, G., Wei, Y., Dahlem, M.A., Wechselberger, M., & Schiff, S.J. (2015). The role of cell volume in the dynamics of seizure,

spreading depression, and anoxic depolarization. *PLoS Comparative Biology*, *11*(8), e1004,414. doi:10.1371/journal.pcbi.1004414.

Wei, Y., Ullah, G., Ingram, J., & Schiff, S.J. (2014a). Oxygen and seizure dynamics: II. computational modeling. *Journal of Neurophysiology*, *112*(2), 213–223.

Wei, Y., Ullah, G., & Schiff, S.J. (2014b). Unification of neuronal spikes, seizures, and spreading depression. *Journal of Neuroscience*, *34*, 11,733–11,743.

Xie, L., Kang, H., Xu, Q., Chen, M.J., Liao, Y., Thiyagarajan, M., O'Donnell, J., Christensen, D.J., Nicholson, C., Iliff, J.J., Takano, K., Deane, R., & Nedergaard, M. (2013). Sleep drives metabolite clearance from the adult brain. *Science*, *342*(6156), 373–377. doi:10.1126/science.1241224.

Yao, W., Huang, H., & Miura, R.M. (2011). A continuum neural model for the instigation and propagation of cortical spreading depression. *Bulletin of Mathematical Biology*, *73*(11), 2773–2790. doi:10.1007/s11538-011-9647-3.

Zamecnik, J., Homola, A., Cicanic, M., Kuncova, K., Marusic, P., Krsek, P., Syková, E., & Vargova, L. (2012). The extracellular matrix and diffusion barriers in focal cortical dysplasias. *European Journal of Neuroscience*, *36*, 2017–2024. doi:10.1111/j.1460-9568.2012.08107.x.

Zandt, B.J., ten Haken, B., van Dijk, J.G., & van Putten, M.J. (2011). Neural dynamics during anoxia and the "wave of death". *PLoS ONE*, *6*, e22,127. doi:10.1371/journal.pone.0022127.